The CYGNSS Level 1 Calibration Algorithm and Error Analysis Based On On-Orbit Measurements

Scott Gleason, *Senior Member, IEEE,* Christopher Ruf, *Fellow, IEEE,* Andrew O'Brien, Darren McKague, *Member, IEEE,*

***Abstract*—The calibration algorithm used by the Cyclone Global Navigation Satellite System (CYGNSS) mission to produce version 2.1 of its Level 1 (L1) science data products is described. Changes and improvements have been made to the algorithm, relative to earlier versions, based on the first year of on-orbit result. The L1 calibration consists of two parts: First, the Level 1a (L1a) calibration converts the raw Level 0 delay Doppler maps (DDMs) of processed counts into received power in units of watts. Second, the L1a DDMs are then converted to Level 1b DDMs of bistatic radar cross section values by unwrapping the forward scattering model, which are then normalized by the surface scattering area to arrive an observation of σ_0. An update to the bottom up term-by-term error analysis is also presented, using on-orbit results to better quantify the accuracy of the rolled-up L1 calibration. The error analysis considers uncertainties in all known input calibration parameters. Lastly, a method for calibrating the time delay of CYGNSS measurements is presented.**

***Index Terms*—Calibration, Scatterometry, GNSS, GPS, Reflectometry, Bistatic Radar, CYGNSS**

I. Introduction and Background

A. The CYGNSS Mission and Instrument

THE CYGNSS mission consists of a constellation of eight satellites equipped with GNSS bistatic radar receivers that map the ocean surface scattered signal power in the vicinity of the specular reflection point using time domain and Doppler frequency filters. The satellites orbit in the same plane at an altitude of approximately 510 km and at an orbit inclination of 35 degrees. CYGNSS acts as a GNSS bistatic scatterometer capable of sensing sea surface mean square slope and near surface winds both in the global ocean and in tropical cyclones, including in high precipitation conditions [1]. Every second the instrument on each observatory outputs four raw delay Doppler maps (DDM) measurements from individual satellite reflections from the Earth's surface.

Each CYGNSS spacecraft carries a Delay Doppler Mapping Instrument (DDMI) capable of locating and tracking GPS signal reflections on the Earth surface and mapping the signal power over a range of time delay and Doppler frequency bins. Each instrument uses two Earth pointing nadir antennas and a single upward (space) pointing zenith antenna for navigation and GPS transmitter calibration [1]. The instrument is passive, using the signals being transmitted from the Global Positioning System (GPS) constellation. The instrument autonomously tracks, and processes the incoming signal to produce reflected signal power over a range of delay and Doppler bins, generating the CYGNSS Level 0 data product [20]. The spacecraft then compresses the DDMs and downlinks them for Level 1 calibration and Level 2 wind speed and mean square slope estimation.

The Level 1 calibration algorithms are applied to each DDM generated by every CYGNSS observatory in the Science Operations Center (SOC). This includes the generation of a near specular point normalized bistatic radar cross section (NBRCS) which is then used in the Level 2 wind speed and surface mean square slope retrieval algorithms.

After this introduction, Section II presents a brief overviews of the Level 1a and Level 1b calibration algorithms, highlighting post-launch changes. Section III presents on-orbit improvements made in the first year of operation of the CYGNSS observatories. Section IV presents an updated error budget, based on on-orbit results, detailing the estimated impact of all known error terms in the Level 1 data products and providing an estimate of the accuracy of the bi-static cross section measurements. Section V includes details on the time delay calibration of the CYGNSS DDM measurements and meta needed to produce a surface range measurement. Section VI includes a brief summary and conclusions.

B. Brief History of GNSS-R Remote Sensing

Using GNSS signals in a bistatic scatterometer-like configuration was first proposed by Hall and Cordy in 1988 [2]. Subsequently, the PARIS altimetry concept was put forward by Martin-Neira in 1993 [3]. Several years later, the first demonstration of wind sensing using GPS reflections was carried out by Garrison, Katzberg and Hill in 1998 from an aircraft [4]. Additionally, several other researchers have performed experiments from near Earth platforms performing wind or wave sensing: [5],[6],[7],[8],[9],[10]. Together, this group of researchers established that GPS signals could be used to sense the near surface ocean wind conditions. In parallel, several researchers were performing GNSS altimetry studies. Additionally, Lowe et al [11] detected a reflected signal from the SIR-C experiment carried on the Space Shuttle. This was followed by the GNSS experiment carried on the UK-DMC satellite which repeatedly detected signals from ocean, land and ice surfaces [12]. The UK-DMC experiment was used to demonstrate sensitivity to wind speed, first in [13], followed by [14]. This was followed by the TechDemoSat (TDS) on-orbit demonstration [15] mission, and subsequently CYGNSS [1]. These results demonstrated that GNSS signals

Scott Gleason is a Project Scientist III at the University Corporation for Atmospheric Research, Boulder, Colorado, USA. email: gleason@ucar.edu

Manuscript accepted May 2018, DOI 10.1109/JSTARS.2018.2832981

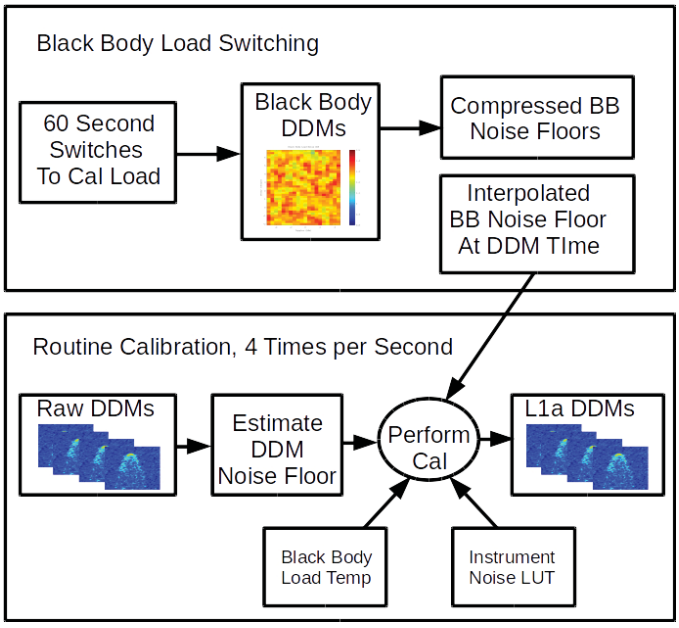

Fig. 1. Overview of CYGNSS Level 1a Calibration.

are easily detectable from a space platform, with the signals clearly responding to surface conditions. A summary of the GNSS-R technique and its applications can be found in [16], [17], [18] and [19].

II. Level 1 Calibration Algorithm Overview

A. Level 1a Algorithm

The Level 1a calibration converts each bin in the Level 0 DDM from raw counts to units of watts. Individual bins of the DDM generated by the DDMI are measured in raw, uncalibrated units referred to as "counts". These counts are linearly related to the total signal power processed by the DDMI. In addition to the ocean surface scattered Global Positioning System signal, the total signal includes contributions from the thermal emission by the Earth and noise generated by the DDMI itself. The power in the total signal is the product of all the input signals, multiplied by the total gain of the DDMI receiver. A block representation of the L1a calibration procedure is shown in Figure 1. The top box shows the periodic generation of black body calibration DDMs which are used during routine DDM calibration. The lower box shows the routine calibration performed on every DDM, 4 times per second. The result is the Level 1a DDM in units of Watts.

The Level 1a algorithms is essentially unchanged from that presented in [21]. By way of comparison, the TDS radiometric calibration algorithm can be found in [22]. However, the initial strategy of updating the instrument noise and gain look-up-tables (LUT) after launch has changed due to difficulties in finding sufficient on-orbit open ocean regions. For this reason the method for updating the look-up-table is being actively redesigned. It has been observed that after one year on orbit, the pre-launch LUT remain within acceptable error limits. However, it is expected the LNA performance will slowly change as the instrument ages further and developing corrections to the existing LUTs are on-going.

B. Level 1b Algorithm

The Level 1a calibrated DDM represents the received surface signal power in Watts over a range of time delays and Doppler frequencies. The CYGNSS Level 1 calibration is designed assuming ocean conditions where diffuse scattering dominates. It is generally understood that at ocean wind speeds greater than 4 m/s this assumption is valid at L-band. At lower wind speeds, the L1 calibration may be subject to errors due to the presence of coherent reflection in the measured signal [34].

Before any geophysical parameters can be estimated these power values must be corrected for non-surface related terms by inverting the forward scattering model. The Level 1b calibration solves for the parameter of interest, the bistatic radar cross section σ. The CYGNSS Level 1b calibration generates two data products associated with each Level 1a DDM: 1) A bin by bin calculation of the surface bistatic scattering cross section, σ (not normalized by scattering area), and 2) bin by bin values of the effective scattering areas (calculated as described below). The normalized bi-static radar cross section σ_0 is then computed from a smaller regions of DDM bins around the specular reflection point and used to estimate near surface winds and mean square slope observables.

The L1a values are corrected for the effects of the transmit and receive antennas, range losses and other non-surface related parameters. An overview of the CYGNSS Level 1b Calibration is shown in Figure 2. The above left box shows a summary of the meta-data collected by the spacecraft and sent to the ground. The flow down from the top right is the estimation of the GPS transmitter transmit powers and GPS antenna gains. The bottom right box show the CYGNSS end-to-end simulator inputs and outputs. All of these elements come together in the middle during the L1b calibration. The down-linked DDMs from CYGNSS consist of 11 Doppler and 17 delay bins. From this DDM, a smaller 5 Doppler by 3 delay bin region around the specular reflection point called the DDM Area (DDMA) is cropped for calculating the per DDM normalized σ_0 value. Details on how this region is cropped is described in Section V(D), with an illustration of the 5 Doppler and 3 delay bins making up the DDMA shown in Figure 8.

Several changes and improvements have been made in the L1b algorithm, which are detailed in the following sections. These changes include; a refined specular point prediction algorithm and determination of the specular point in the DDM measurements, an empirical correction to the CYGNSS receive antenna patterns, a new DDMA weighted cropping algorithm to more accurately capture the received power in the surface measurement region and updated tables of the GPS satellites transmit power and gain generated using zenith navigation signal levels and a ground based GPS Power Monitor. The GPS transmitter corrections, are not discussed in detail here but included in a separate publication [23]. A summary of the GPS transmitter calibration changes is presented here.

III. Level 1 Calibration Improvements

Since the launch of CYGNSS in December 2017, several improvements have been made in the Level 1 calibration

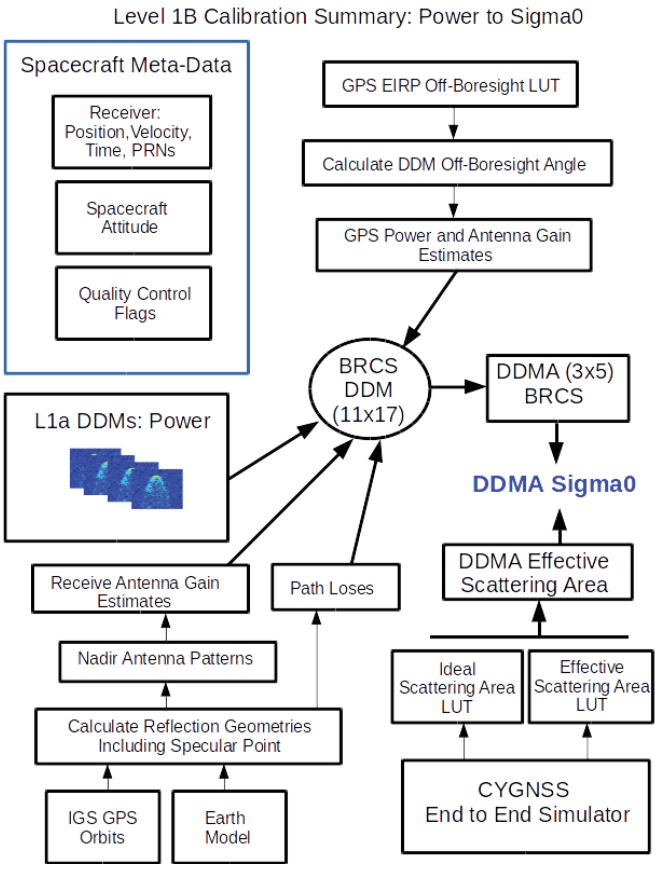

Fig. 2. Overview of CYGNSS Level 1b Calibration.

algorithms, which were initially published in [21]. These updates were based on analysis of the first year of on-orbit data and are individually summarized below.

A. High Accuracy Surface Specular Reflection Point Estimation

The estimated location of the center of the surface glistening zone of the reflected signal provides the main point of reference for the geo-location of the GNSS-R measurement. This point on the surface is referred to as the specular point and can be estimated mathematically using the physical geometry of the transmitting and receiving satellites and a modeled of the Earth's ocean surface. It should be noted that the surface specular point estimation algorithm described below is designed for ocean surfaces. Land specular points over varying topography present unique challenges and will contain additional geolocation errors, not yet accounted for in the current CYGNSS Level 1 calibration.

In the original Level 1 calibration approach, the specular point was solved using a) the position of the receiving satellite, as estimated by the 1Hz single frequency position estimate, b) the estimate of the transmitting satellite using ground based precise ephemeris and c) the WGS84 ellipsoid model of the Earth. This Earth model, although generally accurate enough for most applications, relied on approximations that resulted in residual specular point position estimation errors that where large enough to significantly impact the pixels in the DDM used to calculated the bistatic radar cross section. Subsequently, an improved specular point solver was implemented that used a more accurate DTU10 mean sea surface model [24], combined with a brute force, computationally-efficient specular point solver algorithm.

The specular point on the Earth maps to a single point in the delay-Doppler coordinates in the CYGNSS DDM. The exact specular bin location in the DDM will be located at a fractional pixel location within a single DDM bin. The pixels in the DDM at and surrounding the specular point bin determine the region used to make the surface bistatic radar cross section measurement, the DDMA. The estimation of the DDMA within the Level 1a DDM is described in more detail below using the precise location of the specular point described here. This region of the DDM represents the bins of highest reflected power and smallest spatial footprint on the surface and accurate knowledge of this regions is critical for calibration and wind speed retrievals.

The specular point location on the surface can't be reliably estimated using the peak power bin of the DDM. The peak power pixel results from a combination of effects in addition to the specular point location, including thermal noise, speckle noise or asymmetries in the reflected signal waveform (as a result of geometry and antenna pattern non-uniformity). For this reason, the specular point surface location and location of the specular point in the instrument generated DDM is calculated to a sub-pixel level from first principles (i.e. geometry and timing metadata).

1) Improved Mean Sea Surface Height Model: In order to more precisely predict the specular location, it is necessary to account for deviations in the Earth's mean sea surface height as compared to the WGS84 model. For this purpose, we have utilized the DTU10 mean sea surface model [24]. The mean sea surface is the displacement of the sea surface relative to a mathematical model of the Earth and it closely follows the Earth's geoid. The amplitude of the deviation from the WGS84 ellipsoid is generally within approximately +/- 100 meters over the Earth's ocean surfaces. The original DTU10 data was reduced to a 1 degree by 1 degree resolution to improve the efficiency of the calculation, and which is reasonable, due to the fact that height variations are relatively small. The DTU10 map of sea surface height variations relative to the WGS84 ellipsoid use in the specular point solver is shown in Figure 3.

The height difference, manifests as a path delay error which becomes an error in the predicted location of the specular bin in the DDM. For a typical incidence angle of 30 degrees, a surface height error of 100 meters could result in 170 meters of path delay error. In the CYGNSS DDM, the delay pixel resolution is approximately 0.25 GPS L1 C/A code chips, and one chip corresponds to approximately 293 meters of delay. Therefore, a 170 m path delay error results in the predicted specular bin in the DDM being offset by 2.25 pixels from where we would expect it on the WGS84 ellipsoid.

Figure 4 shows a plot of specular bin delay difference when using DTU10 as opposed to using WGS84. Specular delay differences are shown for 1 day of measurements for 4 satellites (each shown in 4 separate colors). We can observe

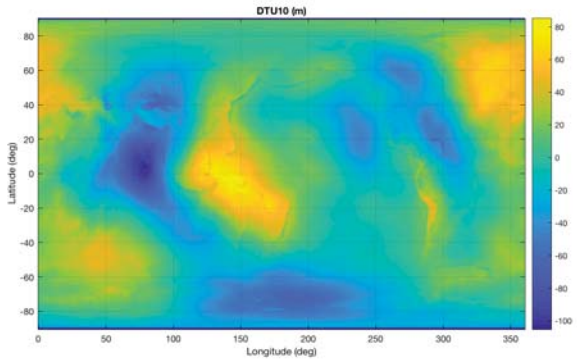

Fig. 3. DTU10 Mean Sea Surface adjustment from WGS84 ellipsoid used for specular point calculation.

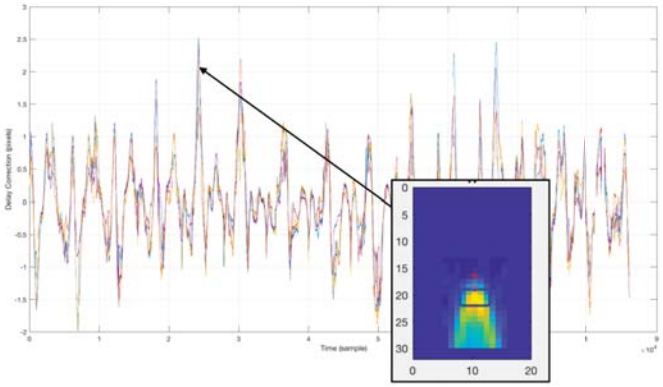

Fig. 4. One day of specular point corrections using the DTU10 model as compared to the WGS84 model. The correction due to the improved specular point solver varies between -2 and 2.5 pixels in delay space in the DDM.

that the delay difference (or correction) due to the improved specular point solver varies between -2 and 2.5 pixels in delay space in the DDM. Figure 4 also shows an example measured CYGNSS DDM. In the DDM, the original specular bin solved using WGS 84 model is shown as a red 'X' while the new specular bin solved using DTU10 is shown with a red square. Visually, it is clear the specular bin location calculated with DTU10 is at the correct location in the reflected waveform. Range errors introduced by incorrect specular point prediction primarily impact the L1 calibration due to misidentifying the correct specular point bins (and specular region reflected power) in the DDM measurements. These errors will also degrade the surface vertical ranging accuracy and horizontal geolocation if not corrected.

2) Specular Point Solver Implementation: The new specular point solution is reported in the CYGNSS Level 1 data in the form of the specular point position and velocity variables. It takes approximately 20 seconds to calculate one day of precise specular points within CYGNSS DDMs from one satellite (approximately 320000 DDMs). The new algorithm used to solve for the specular point is as follows:

1) The original specular point solution based on the WGS84 ellipsoid model is used as our initial estimate of the specular point.
2) A large 3-D grid of points is constructed around the estimated specular point. This grid has uniform latitude and longitude spacing and is conformal to the WGS84 ellipsoid at each point.
3) At each grid point, the DTU10 mean sea surface height is used to shift the altitude. The 1-degree resolution DTU10 data (shown above) is bi-linearly interpolated to find the altitude value at each grid point. The resulting grid is then conformal to the DTU10 surface
4) Next, the point in the grid with the minimum reflection path length (from transmitter to the grid point to the receiver) is found. This minimum-path-delay grid point becomes the new specular point location estimate.
5) An additional higher resolution grid is constructed around this estimated specular point location and steps 2-4 are repeated several times. In this way, a series of search grids sequentially zoom in on the estimated specular point. The choice of initial grid size and resolution are carefully chosen to prevent erroneous convergence.

The specular point we solve for here is defined as the point on the Earth with the minimum reflection path delay. As the surface we use is conformal to an arbitrary geoid topology at each grid point, no mathematical constraint is placed on transmitter and receiver incidence angles in this solution. In a strict sense, it is no longer a "specular" point since (if the ocean surface were smooth) a specular reflection would occur at surface locations with equal transmitter and receiver incidence angles, not minimum delay. Nonetheless, the minimum delay point is sufficiently relevant for our purposes since the corresponding specular bin defines the leading edge of the reflected waveform and the specular point represents the center of our iso-delay surface contours within the reflection glistening zone.

The DTU10 mean surface height model contains data over both ocean and land. The updated specular point estimates are valid and accurate over ocean only, as the DTU10 elevation model does not consider variations in land topography. An additional surface height map will be implemented in future versions of the L1 calibration which includes land surface height variations.

The updated specular point solution is differenced with the instrument estimated specular point solution to produce a correction term in the DDM's delay and Doppler space. This correction is applied to the original prediction of the specular bin location in the DDM during the estimation of the DDMA measurement area, as described in Section V(D).

B. Improved Estimation of Science Antenna Patterns Using CYGNSS Measurements

Prior to launch, antenna pattern measurements were made for all of the port and starboard antennas. In addition, the predicted effects of the spacecraft body where extensively modeled using pattern simulation tools to attempt to accurately predict the final antenna patterns when attached to the spacecraft. These simulations included mechanical CAD models of

the physical spacecraft with electromagnetic field simulations using the FEKO and Savant software packages. and input into Additionally, full pattern measurements of the port and starboard antennas were made while mounted to a CYGNSS Engineering Model (EM) in an anechoic chamber. From the modeling effort, which was confirmed by the EM chamber measurements, we know that the solar panels have a significant impact on the observatory antenna gain patterns.

The individual modeled pattern measurements were adjusted using a constant gain factor based on measured differences between the flight antennas to create the at-launch gain patterns for each CYGNSS flight model (FM) antenna calibration tables.

However, we know that there is potentially significant variability in the exact deployed positions of the solar panels from repeated pre-launch panel deployment tests. It therefore stands to reason that applying a simple constant offset for each of the FM antennas from the modeling and EM measurements is overly simplistic. It was evident from the initial analysis of the CYGNSS on-orbit data that an improved estimate of the CYGNSS antenna patterns was needed for each antenna in the constellation.

1) Estimation of Receive Antenna Gain Error: Analysis of the initial CYGNSS data, released in May of 2017, show a significant dependence of observed σ_0 on the azimuthal observation angle of the specular point with respect to the CYGNSS spacecraft. While the NBRCS values are expected to depend on wind and on incidence angle, the dependence on azimuthal angle was expected to be negligible. These anomalies were quantified in terms of a normalized NBRCS anomaly ($\sigma_{0,anom}$), expressed as:

$$\sigma_{0,anom} = \frac{(\sigma_0 - < \sigma_0 >)}{< \sigma_0 >} \tag{1}$$

σ_0 is expected to vary as a function of wind speed and geometry, so σ_0 anomalies are computed as the difference between each calibrated σ_0 from the mean value for all σ_0 within 2 meters per second wind speed and 2 degree incidence angle bins. Reference wind speeds are from collocated ECMWF reanalysis fields to within 90 minutes and 25 kilometers of the corresponding CYGNSS observations. To determine the dependence of these anomalies on azimuth angle, average anomalies were computed in 1 degree azimuth bins. The results using the original calibration algorithm between day of year 77 and 121 are shown in Figure 5. Results are averaged across all 8 CYGNSS satellites for the starboard and port antennas. For this and future analysis shown, the average of the σ_0 in the DDM is computed using the estimates $sigma_0$ over the DDMA region near specular point DDM bins. It is important to note that due to the cross track ground projection of the receive antenna patterns and on-board track selection algorithm, most of the measurements are distributed within 30 degrees in azimuth angle around 90 degrees (for the Starboard) and 270 degrees (for the Port) measurement orientations.

The key variables in the Level 1b calibration are the transmit power P^T , transmit antenna gain G^T_{SP}, the receiver antenna gain G^R, and geometric factors including the range correction R^{Total}_{SP}. Additionally, the effective scattering area used to normalizing σ also contributes to the overall level of σ_0. Of these, only the antenna gain patterns G^T and G^R depend directly on azimuthal angle. The transmit antenna gain G^T will vary from observation to observation, but not in a manner highly correlated with specular point azimuth with respect to the CYGNSS spacecraft. Therefore, it was hypothesized that the likely candidate for the observed azimuthal variation was the receiver antenna gain G^R.

2) Improved CYGNSS Antenna Patterns: On-orbit estimates of $\sigma_{0,anom}$ described above have been calculated for all CYGNSS flight antennas. For each flight antenna in the constellation (1 port and 1 starboard antennas for each of 8 spacecraft = 16 total antennas), $\sigma_{0,anom}$ anomalies were computed in 1 degree increments of spacecraft off-nadir and azimuth angle. These antenna correction maps were then smoothed over 5 degree windows in azimuth and off-nadir angle in order to reduce measurement noise.

These results were then interpolated using nearest neighbor interpolation to a resolution of 0.1 degree. This map of $\sigma_{0,anom}$ as a function of antenna coordinates was used to scale the original patterns to produce a new estimate of the receive pattern gain, which greatly reduced the observed azimuthal anomalies (anomaly subtracted from original antenna pattern in logarithmic space from estimates of gain in dB). This was done for all 16 operational flight antennas on all 8 observatories.

The resulting $\sigma_{0,anom}$ anomalies gain maps as a function of azimuth averaged across all 8 spacecraft is shown in Figure 5. The anomalies, which were initially greater than as 40% are reduced to less than 20% residual anomalies across all azimuth angles. The regions near the azimuth angles where most measurements are taken (90 and 270 degrees for Starboard and Port, respectively) have errors reduced to 10% or less. The remaining errors are most likely due to variability within the data not related to wind speed, incidence angle, or receiver antenna pattern effect accounted for in this analysis.

It should also be noted that off-nadir angle is highly correlated to incidence angle for a given spacecraft orientation, with the relationship directly tied to the spacecraft roll, which changes periodically as the spacecraft are adjusted to maintain a power positive orientation for high solar beta angles.

An example of the original pre-launch CYGNSS receive antenna gain patterns for the CYGNSS FM1 starboard antenna and gain corrections applied are shown in Figure 6.

C. Digital to Analog DDM Scaling Issue

In the original CYGNSS L1a calibration algorithm, the entire Level 1a DDM was scaled from digitally sampled DDM values to the equivalent analog sampled power based on the 2-bit analog to digital sample distribution. This correction was based on well known methods in radio astronomy for dealing with finite digital sampling of analog signals. However, examination of closely geo-located tracks between different observatories at very close time intervals revealed an observed bias between measurements over nearly identical conditions. Figure 7 (top) shows one such case, where FM6 and FM8 pass over nearly the same surface within 5 minutes of each other,

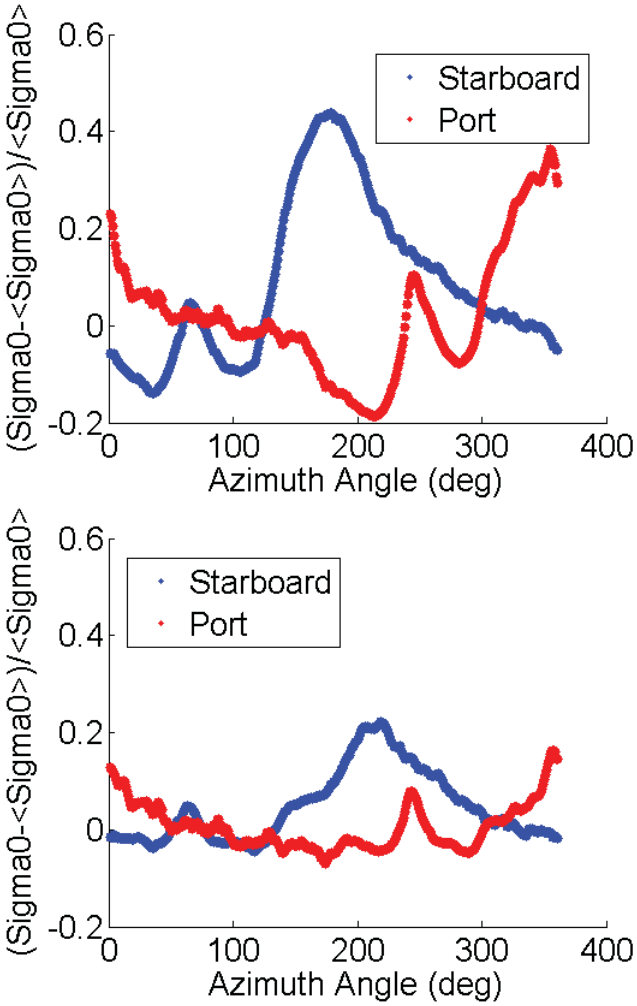

Fig. 5. (above) σ_0 anomalies computed for Level 1 data between day of year 77 and 121 of 2017 on the Version 1 using pre-launch estimated receive antenna patterns. (below) σ_0 anomalies computed for Level 1 Corrected data for Version 2 of the L1 calibration. The anomalies reduce the worst case error of 40% to less than 10%.

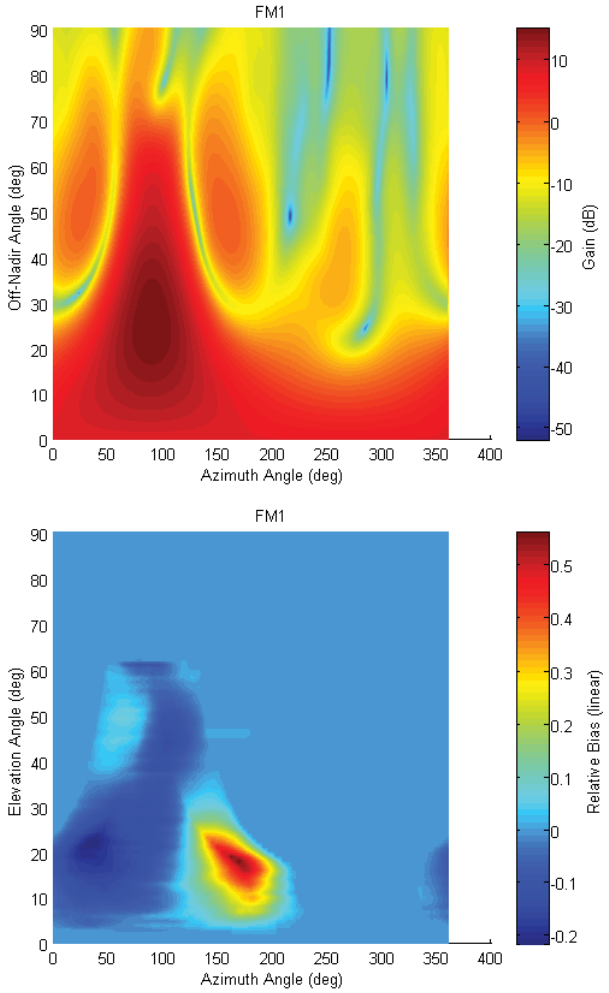

Fig. 6. (above) Original FM1 starboard antenna pattern. (below) FM1 starboard antenna pattern corrections applied to produce the improved FM1 starboard antenna pattern.

yet a clear difference in the NBRCS values can be observed over the length of the track. Upon subsequent investigation, an issue in the analog to digital scaling being applied was found, in which the calculated correction between digital and analog measurements was not correct and introducing significant statistical biases between observatories.

Upon removal of the existing digital to analog scaling the overall inter-satellite bias statistics improved significantly. Figure 7 (bottom) shows the same two tracks after the scaling has been removed, with good agreement across the entire track.

The exact problem with the digital to analog scaling is being investigated and has not yet been identified. However, as a significant reduction in inter-satellite measurement bias was demonstrated with the removal of the digital to analog scaling factor, it will be included in the next public data release.

D. Improved DDMA Calculation Using Adjacent Bin Weighting Algorithm

The Level 1b bin by bin DDM of σ and the bin by bin DDM of effective scattering areas can be combined to calculate a normalized radar cross section value, σ^0, over selected regions of the measurement DDM called the DDMA. The CYGNSS Level 2 wind retrieval products use the DDMA to generate geophysical model functions (GMF) to estimate near surface winds. . The DDMA consists of 3 delay bins and 5 Doppler bins, with the specular point located in the top (shortest delay) row of this region. Figure 8 shows this DDMA region in red, overlapped with the normal instrument processed DDM delay and Doppler pixels. The true (best estimate) center of the DDMA region (as calculated by the precise specular point estimation method described above) is marked as a red dot in this figure, while the white dot is the center of the Level 1b DDM that the ”true” center falls in.

These ”true” DDMA bins will not normally align exactly with the L1b DDM bins generated by the instrument (due to errors in the instruments open loop signal tracker) making a simple summation over 15 total bins in the L1b DDM problematic. The ”true” DDMA radar cross section is the weighted combination of L1b DDM bins around the best estimate surface specular point and fractional contributions from bins around the edge of the DDMA region. This set of

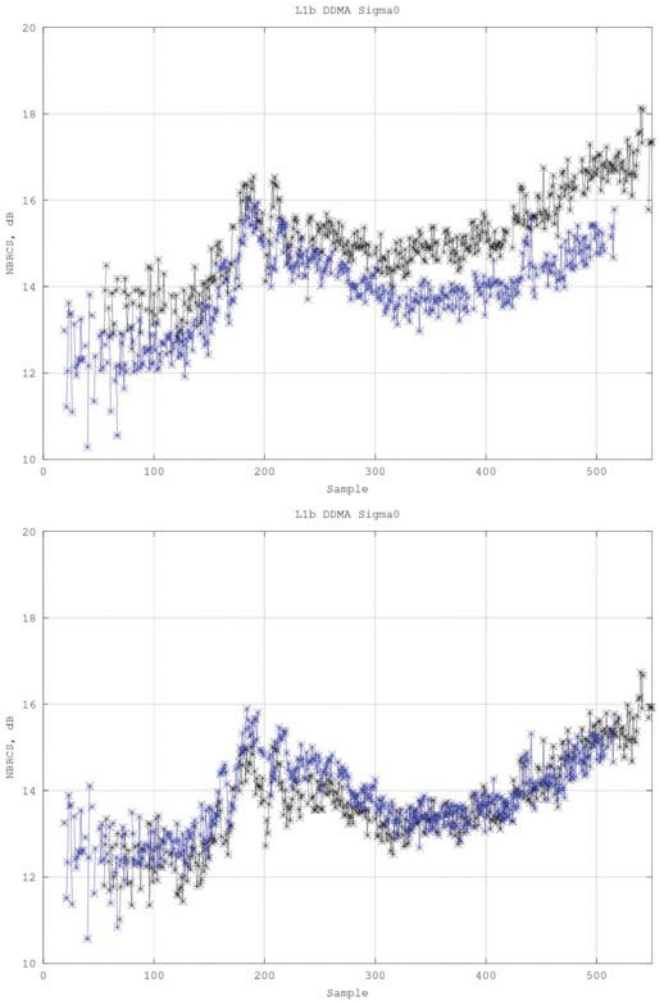

Fig. 7. (top) Inter-satellite bias between tracks of FM6 and FM8 on August 23rd less than 5 minutes apart. (bottom) After digital to analog scaling removed NBRCS values agree much better across the same ocean track.

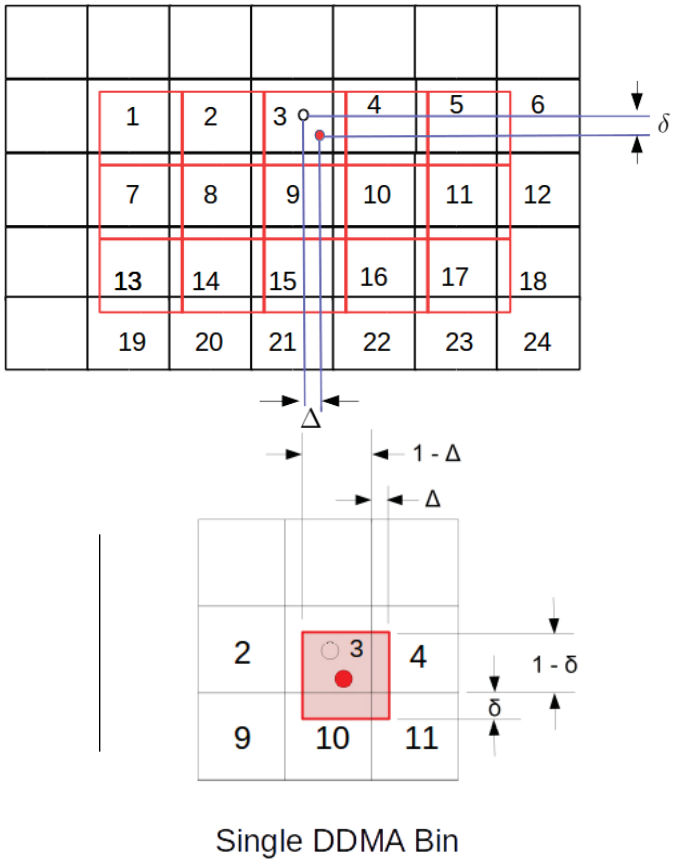

Fig. 8. (top) Level 1b DDM of σ values. Numbered to corresponding to same pixels with DDMA overlayed and bin numbers referenced to Equation 3. The red group of DDMA bins is the overlay of the 3 by 5 DDMA measurement area with the processed DDM pixels, containing a typical mis-alignment. The best estimate DDMA, is based on a refined specular point estimate and represents the true measurement error. (bottom) Detail of the overlap areas of a single DDMA bin (the specular point bin) and adjacent L1b bins.

DDM bins centered around the best estimated fractional bins value is, when weighted and summed, the best estimate of the "true" multi-bin DDMA total radar scattering cross section σ_0 . The mis-alignment between the measured L1b DDM bins and the "true" DDMA bins is illustrated in Figure 8. The DDMA center is offset by fractional bin amounts in delay (δ) and Doppler (Δ) from the L1b measurement DDM shown in the figure.

In order to calculate the total radar cross section in the red DDMA area, the actual measurement L1b values (one per white box/pixel) need to be combined using a weighting scheme that includes only a fractional amount of power from bins around the edges of the DDMA bins. The fractional weighting scheme used is approximated to be linear in both the delay and Doppler dimensions. Figure 8 shows the regions of overlap for a single red DDMa bin with respect to the surrounding measurement bin values.

The total DDMA radar cross section can be calculated as per Equation 2, resulting in a combined expression for the DDMA σ^0,

$$\sigma^0 = \frac{\sigma_{weighted}}{A_{total}} = \frac{W_{i,j} \sum_{i=1}^{N} \sum_{j=1}^{M} \sigma_{\tau_i, f_j}}{\sum_{i=1}^{N} \sum_{j=1}^{M} A_{\tau_i, f_j}} \tag{2}$$

where N and M represent the delay and Doppler bin in the L1b DDM, respectively (with N = 4 and M = 6, a single bin more than the DDMA size in both dimensions).

$$\begin{aligned} \sigma_{weighted} = {} & (1-\delta)(1-\Delta)\sigma_1 + (1-\delta)(\sigma_2+\sigma_3+\sigma_4+\sigma_5) \\ & + (1-\delta)\Delta\sigma_6 + (1-\Delta)(\sigma_7+\sigma_{13}) + \Delta(\sigma_{12}+\sigma_{18}) \\ & + \delta(1-\Delta)\sigma_{19} + \delta(\sigma_{20}+\sigma_{21}+\sigma_{22}+\sigma_{23}) + \delta\Delta\sigma_{24} \\ & + (\sigma_8+\sigma_9+\sigma_{10}+\sigma_{11}) + (\sigma_{14}+\sigma_{15}+\sigma_{16}+\sigma_{17}) \end{aligned} \tag{3}$$

Each bin in the L1b DDM contributing to the weighted $\sigma_{weighted}$ is scaled by a weighting factor $W_{i,j}$ based on the overlap with the respective "true" DDMA bin. $\sigma_{weighted}$ is then normalized by the sum of the effective area DDMA bins (which are centered at the ideal specular reflection point and require no weighting correction) to arrive at the final σ^0 measurement over the "true" DDMA region. The summations and weighting involved in calculating $\sigma_{weighted}$ for the example

above is expressed in Equation 3, where the delay and Doppler index values are simplified to single bin numbers as illustrated in Figure 8, and terms with the same weighting factor are combined.

E. Generating Improved GPS Transmit Power and Antenna Gain Look Up Tables

The GPS Transmit Power, P_T and transmit antenna gain, G_T, or the effective isotropic radiated power (EIRP) can be estimated using a parametrized model as a function of the transmitter space vehicle (SV) for all GPS satellites. Initial antenna patterns were originally previously published for the Lockheed Martin satellite blocks [25]. These patterns provided no information on the transmit power of the satellites, only the gain, which introduced significant errors in the L1b calibration due to uncertainties in this parameter.

After launch, the individual per satellite EIRP values were estimated using a ground based GPS Power Monitor located at the University of Michigan. Additionally, the signal to noise ratio of signals tracked by the zenith antenna navigation channels were used to invert power and pattern estimates for GPS constellation satellites. Over time, it was possible to generate transmit power estimates and antenna gain maps for all operational GPS satellites over a full range of reflection geometries.

More details on how these new GPS EIRP maps were generated is described in more detail in [23]. In the Version 2.0 Level 1 data product release, improved estimates of the individual GPS transmit powers were included, as well as updated to the pre-launch off-boresight antenna pattern corrections. Future version of the GPS EIRP update will include azimuthal variation corrections of the GPS antenna patterns as well as constant monitoring and validation of unannounced changes to the GPS transmit power levels. The GPS yaw angle is predictable using existing models (such as [26]), while the nominal GPS satellite roll and pitch angles are assumed to be nominally Earth pointing.

IV. CYGNSS Level 1 Error Estimation Method

This analysis assumes that the uncertainties in the CYGNSS Level 1 calibration algorithm are generally independent uncorrelated error sources, which can be characterized with a zero mean Gaussian distribution. This may not be strictly the case for some terms (most notably the GPS transmit power levels), yet to a first order this analysis serves to bound the expected error and as shown in the top-down analysis in Ruf et al [27] is consistent with the best estimate of the overall on-orbit observed CYGNSS wind retrieval performance. The method for this error analysis is based on the partial derivative method presented in Jansen et. al [28]. Additionally, the rolled up error was simulated using a Monte Carlo simulation and was in agreement with the partial derivative estimated error levels presented below.

For more details on the partial derivatives for individual error terms in the L1a and L1b calibration equations refer to Gleason et al [21].

A. Error Analysis Methodology

The total error in the L1a or L1b calibrated DDM is the root of sum of squares (RSS) of the individual errors sources in the independent terms of their respective expressions, which can be expressed generically as,

$$\Delta L_1^{a,b} = \left[\sum_{i=1}^{x} [E(q_i)]^2 \right]^{1/2} \tag{4}$$

where $L_1^{a,b}$ are the L1a and L1b estimated error values, x is the number of independent errors terms and q_i are the respective input error parameters. The individual errors terms can be estimated by taking the partial derivatives of the calibration equation such that each error term in the process can by quantized as,

$$E(q_i) = \left| \frac{\partial L_1^{a,b}}{\partial q_i} \right| \Delta q_i \tag{5}$$

B. Quantifying Level 1a Errors

The expression for the L1a DDM is shown in Equation 6, from [21], and can be substituted into Equation 5 to estimate the rolled up L1a error of the estimated received power P_g, as a function of individual input terms.

$$P_g = \frac{(C - C_N)(P_B + P_r)}{C_B} \tag{6}$$

Where the individual L1a error terms are defined as: $p_1 = C$, $p_2 = C_N$, $p_3 = P_B$, $p_4 = P_r$ and $p_5 = C_B$. Following, ΔC is the error inherent in the Level 0 DDM counts, ΔC_N is the error in the estimate of the normal DDM noise floor, ΔP_B is the error in the estimate of the black body load DDM noise power, ΔP_r is the error in the temperature vs LNA noise figure look up table and ΔC_B is the error in the estimate of the black body DDM noise floor.

The 1-sigma uncertainties in these quantities are expressed as Δp_i. The L1a 1-sigma uncertainties and the resulting partial derivative error terms are shown in Table I.

How each of the 1-sigma error levels in Table I was arrived at is described below.

1) ΔC is the combination of the quantization error (negligible) and non-common mode contributions to the signal counts. The later can include cross correlations with other GPS satellites which would not effect the signal and noise floors equally and cancel out in the L1a calculation made in Equation 6. Although not possible to accurately quantify exactly the error that may be introduced in the actual data, simulations showed that as a worse case, for certain PRN cross correlations, this error could be up to 0.1 dB.
2) ΔCN is driven by the number of noise bins averaged during the routine calibration. This method has not changed from the analysis presented in [21]. However, the more conservative high wind speed value of 0.14 dB is used to better bound the error and to account for the possibility for mild RFI levels which would not be detected by the RFI detection algorithm.

Error Term	Error Magnitude, dB	Comment
	At 10 m/s Reference Wind	
$E(C)$	0.10	Quantization and non-common mode interference
$E(CN)$	0.14	DDM Noise Floor (45 row by 20 pixel average)
$E(PB)$	2 degrees C	Calibration Load Noise Power (from load temperature)
$E(Pr)$	0.14	Instrument Noise Power (from pre-launch LUT uncertainty)
$E(CB)$	0.05	Calibration Load DDM Noise Counts
Total RSS L1a Error	0.13	From Partial Derivatives and MC Simulation

TABLE I
ESTIMATES LEVEL 1A 1-SIGMA UNCERTAINTIES, INDIVIDUAL ERROR CONTRIBUTIONS AND ROLLED UP L1A ERROR ESTIMATE.

3) ΔPB is determined by the accuracy of the temperature sensor on the black body calibration load.
4) ΔPr was calculated from the 1-sigma variation in the pre-launch raw measurements used to generate the instrument noise figure vs temperature look up table.
5) ΔCB is estimated from the expected error after averaging a full black body calibration DDM (128 rows by 20 columns) every 60 seconds. Includes a small error component due to the propagation to the DDM measurement time between 60 second switches to the calibration load.

C. Rolled Up On-Orbit Level 1 Calibration Errors

The wrapped up errors of the Level 1b calibration can be expressed in a similar manner, with the total L1a error rolled in, and estimated over the DDMA region of the DDM (3 delays x 5 Dopplers),

$$\bar{\sigma}^0_{DDMA} = \frac{P_{g,DDMA}(4\pi)^3 L_{atm}}{P^T \lambda^2 G^T_{SP} G^R_{SP} R^{Total}_{SP} A_{DDMA}} \tag{7}$$

Substituting this equation into Equation 5 results in,

$$E(q_i) = \left| \frac{\partial \bar{\sigma}^0_{DDMA}}{\partial q_i} \right| \Delta q_i \tag{8}$$

Where the errors terms are: $q_1 = P_g$ (rolled up L1a errors), $q_2 = DDMA_{crop}$, $q_3 = L_{atm}$, $q_3 = R^{Total}_{SP}$, $q_4 = P_T$, $q_5 = G^T$, $q_6 = G^R$ and $q_7 = A$, respectively.

The On-orbit estimated rolled up Level 1 calibration error is shown below II with 1-sigma error estimates for each term.

1) $E(P_g)$ is the rolled up L1a error from Table I.
2) $E(DDMA_{crop})$ is an estimate of the error in the DDMA Weighting algorithm detailed above. The weighting algorithm uses a linear interpolation over non-linear DDM bins and this will introducs some error in the cropping of the final value. The value of 0.1 dB is an approximation based on ideal simulations of the DDMA weighting algorithm.
3) $E(L_{atm})$ is an estimate of the atmospheric attenuation over the signal path. Due to its L-band frequency, the atmospheric attenuation errors are expected to be very small [31].
4) $E(R^{Total})$ is the total error due to mis-estimation of the path loss from the GPS transmitter to the specular point to the receiver. Given the relatively high accuracies of all three of these parameters, this error is expected to be negligible. More details on the contribution due to the single frequency GPS receiver position estimation performed on CYGNSS can be found in [29] and [30].
5) $E(P_T)$ + $E(G^T)$ is the error in the GPS transmit power and antenna gain correction. The best estimate for this error is based on analysis of the GPS Power Monitor determination of the GPS transmit powers [23] and the top down analysis reported in [27].
6) $E(G^R)$ is the error in the receive antenna gain and is based on the analysis of σ_0 anomalies described above, after the described corrections to the receive antenna patterns were applied. The antenna gain error was estimated using Monte Carlo simulations based on the predicted statistical spacecraft attitude performance and best estimate of the receive antenna gain pattern, described in more detail in [21].
7) $E(A)$ is the estimated error in the effective scattering normalization area used to convert σ to σ_0. The CYGNSS End-to-End Simulator was used to generate the look-up-tables used to generate these values. Given the extensive validation of the E2ES this error was at a relatively low value, driven by errors introduces due to the integration step size used in the table generation, plus a small amount of margin.

V. TIME DELAY CALIBRATION OF CYGNSS DATA

This section contains a summary and example of how to interpret the CYGNSS DDM measurements and meta data to estimate the precise time delay of the specular reflection point. Custom methods can be developed independently using the parameters described below for various applications.

The CYGNSS instrument was primarily designed for ocean scatterometery applications. This results in a number of inherent limitations to making a precise range measurement with CYGNSS. These limitation will not prevent range measurements from being made but may degrade the achievable accuracy. These limitations include,

1) The CYGNSS DMR processes only DDMs from the GPS L1 C/A signal. The bandwidth of this signal will place some fundamental limitations on the ranging accuracy, when compared to the effective received signal bandwidth of a traditional "chirp" radar altimeter or the higher bandwidth GNSS signals [32]. The CYGNSS GPS L1 C/A single "chip" length is approximately 293 meters, with a 2 MHz bandwidth.

Error Term	Error Magnitude, dB	Comment
	At 10 m/s Reference Wind	
$E(P_g)$	0.13	Rolled Up L1a Error (from above)
$E(DDMA_{crop})$	0.1	Error in DDMA Weighting Algorithm
$E(L_{atm})$	0.04	Atmospheric Losses
$E(R^{Total})$	2000 meters	Total range error
$E(P_T)$ + $E(G^T)$	0.24	GPS Transmitter EIRP error from top-down analysis [**?**]
$E(G^R)$	0.25	Estimated Receiver Antenna Gain Error From MC Simulation
$E(A)$	0.05	Effective Scattering Area Error, From E2ES
Total RSS L1b Error, dB	0.39	Rolled Up L1b Error (Without Margin) From Partial Derivatives and MC Simulation

TABLE II
ROLLED UP LEVEL 1B CALIBRATION ALGORITHM ESTIMATED ERRORS.

2) The CYGNSS instrument includes only a single frequency navigation receiver. Applications which require precise orbit determination (POD) solutions to produce a centimeter level estimate of the satellite position will need to perform additional processing on the CYGNSS navigation data to improve the CYGNSS navigation receiver accuracy, which is in on the order of 10s of meters.
3) The maximum CYGNSS nadir antenna gain is approximately 15dB, which is generally considered low for capturing the high SNR levels needed to perform submeter ranging from a rough surface reflection.

Nevertheless, it is still possible to make surface delay measurements with CYGNSS. The CYGNSS constellations high temporal and spatial revisit times may provide unique advantages over existing instruments, even with reduced ranging accuracy. A sea surface height application which may be possible with CYGNSS is the observation of Oceanic Rossby Waves, and there interaction with mesoscale variability over local regions. Existing altimeters can't provide the temporal coverage CYGNSS measurements provide. Additionally, very high accuracy is not required, as even very noisy, but very dense observations would be useful to observe these interactions. Thus CYGNSS measurements, possibly anchored to an existing traditional pulsed radar instrument would provide improved observation of ocean events which occur and dissipate quickly, and are very difficult to observe with existing radar altimeters [33].

A. CYGNSS Metadata Relevant to GNSS-R Delay Calibration

CYGNSS Level 1 products contain meta data which can be used for delay calibration of the DDMs. Note that, often there will be "ddm" and "pvt" suffixes for the same parameters. The "ddm" suffix indicates that the variable has been linearly interpolated to the mid-point of the DDM non-coherent integration interval, while the "pvt" suffix indicates the value calculated by the instrument at the 1Hz position/velocity/time (PVT) epoch of the navigation receiver. Unless otherwise stated below the variables listed are at "ddm" time. A list of netCDF variables with application to GNSS-R delay calibration include (netCDF variables names and symbols for subsequent equations appended):

1) CYGNSS observatory position (WGS84). netCDF variables: sc_pos_x, sc_pos_y, sc_pos_z. ($\hat{R}_{pos}$)
2) Precise ground estimate of specular reflection point. netCDF variables: sp_pos_x, sp_pos_y, sp_pos_z. ($\hat{S}_{pos}$)
3) Precise ground estimate of transmitter position. netCDF variables: tx_pos_x, tx_pos_y, tx_pos_z. ($\hat{T}_{pos}$)
4) Direct signal code phase from the navigation receiver "prompt" tracking correlator. netCDF variable: zenith_code_phase. (ψ) .
5) Instrument estimated additional path from the direct signal code phase to the open loop tracked specular reflection point of the DDM. netCDF variable: add_range_to_sp. (ϕ^{DMR})
6) Integer bin delay and Doppler offsets applied to the instrument open loop tracking center applied by the on-board DDM compression algorithm. netCDF variables: fsw_comp_delay_shift, fsw_comp_dopp_shift. ($\Delta_{SP}^{FSW}, delayshift$)
7) Ground estimated precise specular point delay and Doppler bin locations in the DDM. netCDF variables: brcs_ddm_sp_bin_delay_row brcs_ddm_sp_bin_dopp_col. ($\alpha_{SP}^{delay}, delaybin$)
8) Delay and Doppler bin resolution of the DDM. Nominally 0.25 C/A code chips and 500 Hz. netCDF variables: delay_resolution, dopp_resolution. (δ, delay resolution)
9) Instrument clock bias and bias rate, which can be used to make small correction to clock frequency and bin resolutions. Nominal instrument clock frequency is 16036200 Hz. netCDF variables: rx_clk_bias, rx_clk_bias_rate.

Intermediate variables which are not included in the netCDF, but used in the estimation of the specular point location in the DDM include; a) ϕ^{SOC}, which is the higher accuracy re-calculation of the additional range to the specular point variable ϕ^{DMR}, calculated in real-time on the instrument. b) Δ_{SP}^{corr}, which is the range difference (or correction) between the instrument and ground estimated values of the additional range to the specular point.

The SOC calculations for the precise specular point delay bin and C/A code phase are included below. The Doppler bin can in theory be re-calculated in a similar manner, however, in practice the Doppler bin of the specular point has proven to be consistently located in the center DDM Doppler bin.

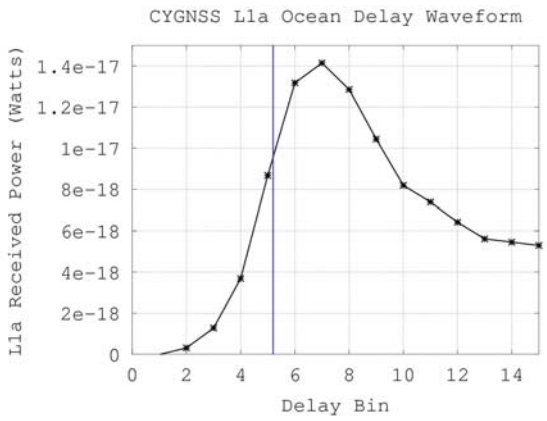

Fig. 9. Example of ground estimated specular point location in CYGNSS delay waveform.

B. Calculating Specular Point Delay Bin and Code Phase Reference

Figure 9 shows a typical CYGNSS delay waveform over the ocean, including a "slice" of all delay bins at the center Doppler bin. The vertical line on the delay axis is the estimated specular point delay bin calculated using the ground estimated precise specular point location. The precision delay bin offset of the specular point in the DDM is calculated as,

$$\alpha_{SP}^{delay} = \frac{16 - \Delta_{SP}^{corr}}{\delta} - 8 - \frac{16 - \Delta_{SP}^{FSW}}{\delta} \tag{9}$$

Where, α_{SP}^{delay} is the ground calculated specular point delay bin estimate ($brcs\_ddm\_sp\_bin\_delay\_row$), 16 is the max delay bin (0 base bin numbering), Δ_{SP}^{corr} is the ground estimated error in the Instrument open loop tracker specular point center, Δ_{SP}^{FSW} is the delay shift applied by the on-board compression algorithm and δ is the DDM delay bin resolution.

This value represents the ground estimated specular reflection point location in the CYGNSS delay waveform. From this reference point all delays before and after the estimated specular point delay bin can be computed using the fixed delay resolution steps (ideally corrected using the clock error terms).

C. Linking the Delay Waveform Bins with an Absolute C/A Code Phase

We can then link the bins of the CYGNSS delay waveform to absolute values of the transmitted C/A code phase by using the zenith signal navigation code phase as a reference. The absolute C/A code phase of the ground estimated specular point delay bin can be expressed as,

$$\Gamma_{SP}^{DMR} = \psi + \frac{\phi^{DMR}}{\chi} \tag{10}$$

Where, Γ_{SP}^{DMR} is the open loop tracker estimated GPS C/A code phase at the specular point delay bin estimate, ψ is the direct (zenith) navigation signal close loop tracked C/A code phase, ϕ^{DMR} is the additional range to the specular point coarse estimated made in real-time on the instrument and χ is the meters in a single GPS C/A chip. This value is recalculated on the ground using the higher accuracy estimate of the specular point location as,

$$\Gamma_{SP}^{SOC} = \psi + \frac{\phi^{SOC}}{\chi} \tag{11}$$

Where, Γ_{SP}^{SOC} is the Science Operations Center (SOC) estimated C/A code phase of the specular point in the compressed instrument DDM and ϕ^{SOC} is the SOC estimated additional range to the specular point made using the ground based precise specular point estimation.

The SOC estimated specular point delay error is the difference between the real-time instrument estimated specular point delay and the SOC estimated delay, expressed in meters as,

$$\Delta_{SP}^{corr} = (\Gamma_{SP}^{SOC} - \Gamma_{SP}^{DMR})\chi \tag{12}$$

This value is then substituted into Equation 9 to calculate the precise delay bin of the specular point in the DDM, which also includes corrections for the flight software compression algorithm delay shift.

D. Estimating the Additional Range to the Specular Point

The SOC estimated additional range to the specular point (ϕ^{SOC}), includes a high precision specular point estimator calculated using an iterative solver and a local region digital elevation map as described above. This value can then be used in combination with the estimated CYGNSS receiver and GPS transmitter positions to estimate the additional range to the specular point (relative to the zenith signal) as,

$$\phi^{SOC} = \left[\|\hat{T}_{pos} - \hat{S}_{pos}^{SOC}\| + \|\hat{R}_{pos} - \hat{S}_{pos}^{SOC}\|\right] - \|\hat{T}_{pos} - \hat{R}_{pos}\| \tag{13}$$

Where, $\hat{T}_{pos}$ is the GPS transmitter position coordinates, $\hat{R}_{pos}$ is the CYGNSS observatory position and $\hat{S}_{pos}^{SOC}$ is the SOC estimated precise specular point position.

Its is, of coarse, possible to develop other specular point location estimators, and refine the receiver position estimate, which can then be used in the Equations above to re-estimate the specular delay bin location in the DDM.

E. Using a GNSS-R Model to Estimate the Mean Surface Height on the Delay Waveform

Generally, GNSS-R ocean surface height estimation is often performed using a delay or DDM model fitting technique using a GNSS-R specific scattering model, such as that of Zavorotny and Voronovich, [34]. The model can be used to improve the estimate of the mean sea surface height location using an optimal least squares fit or matched filter approach. This will potentially result in an improved surface range estimates over the CYGNSS delay waveform or DDM. This technique follows the same general methodology as applied to "chirp" pulses from traditional radar altimetry instruments. In traditional pulsed compress radar altimeter a commonly

used model is that published by Brown [35]. Using a similar approach in GNSS-R, while applying a GNSS-R specific mode, will permit further refinement of the specular point delay bin location and C/A code phase of the predicted sea surface height. This can then be linked to the CYGNSS DDM measurements using the provided reference delay (vertical line in Figure 9) and the known delay bin spacing.

VI. Summary and Conclusions

This paper has given a brief overview of the CYGNSS Level 1 calibration algorithms, detailing changes made after launch with respect to the initial design presented in [21]. Details of the significant changes from the pre-launch algorithms were presented and demonstrated with on-orbit data. An updated error analysis was presented based on the first year of on-orbit results of the CYGNSS observatories. The resulting error analysis estimates that the rolled up Level 1 RMS error of the normalized bistatic radar cross section, σ_0, values over the near specular DDMA region of CYGNSS measurements to be 0.39 dB. Finally, an overview of how the CYGNSS measurements are calibrated with respect to a precise time delay reference was presented.

References

[1] Ruf, C., R. Atlas, P. Chang, M. Clarizia, J. Garrison, S. Gleason, S. Katzberg, Z. Jelenak, J. Johnson, S. Majumdar, A. OBrien, D. Posselt, A. Ridley, R. Rose, V. Zavorotny, "New Ocean Winds Satellite Mission to Probe Hurricanes and Tropical Convection," Bull. Amer. Meteor. Soc., doi:10.1175/BAMS-D-14-00218.1, 2015.

[2] Hall, C., and Cordy, R.,"Multistatic Scatterometry". In Proceedings of the IEEE International Geoscience and Remote Sensing Symposium , Edinburgh, Scotland, 1988.

[3] Martin-Neira, M., "A passive reflectometry and interferometry system (PARIS): Application to ocean altimetry", ESA Journal, vol. 17, pp. 331355,1993.

[4] Garrison, J.L., Katzberg, S.J., and Hill, M.I., "Effect of Sea Roughness on Bistatically Scattered Range Coded Signals from the Global Positioning System," Geophysical Research Letters, Vol. 25, No. 13, pp. 2257-2260, July 1 1998.

[5] Soulat, F., Sea Surface Remote Sensing With GNSS and Sunlight Reflections. PhD Thesis. Universitat Politecnica de Catalunya, 2004.

[6] Germain, O., Ruffini, G., Soulat, F., Caparrini, M., and Silvestrin, P., "The Eddy Experiment II: GNSS-R Speculometry for Directional Sea Roughness Retrieval from Low Aircraft," Geophysical Research Letters, Vol. 31, No.21, 2003.

[7] Cardellach, E., Ruffini, G., Pino, D., Rius, A., Komjathy. A., and Garrison, J.,"Mediterranean Balloon Experiment: Ocean Wind Speed Sensing From the Stratosphere Using GPS Reflections," Remote Sensing of Environment, 88 (2003) pp. 351-362.

[8] Armatys, M., Estimation of Sea Surface Winds Using Reflected GPS Signals. Ph.D. Thesis, University of Colorado at Boulder, 2001.

[9] Komjathy, A., Zavorotny, V.U., Axelrad, P., Born, G.H., and Garrison, J.L., "GPS Signal Scattering from Sea Surface: Wind Speed Retrieval Using Experimental Data and Theoretical Model," Remote Sensing of Environment, Vol. 73, pp. 162174, 2000.

[10] Katzberg, S.J., and J. Dunion, "Comparison of reflected GPS wind speed retrievals with dropsondes in tropical cyclones," Geophysical Research Letters, Vol. 36, L17602, doi:10.1029/2009GL039512., 2009.

[11] Lowe, S., LaBrecque, J.L., Zuffada, C., Romans, L.J., Young, L.E., and Hajj, G.A., "First Spaceborne Observation of an Earth-Reflected GPS Signal," Radio Science, Vol. 37, No. 1, 2002.

[12] Gleason S., Hodgart S.,Yiping S.,Gommenginger C.,Mackin S.,Adjrad M. and M. Unwin (2005), "Detection and Processing of Bistatically Reflected GPS Signals from Low Earth Orbit for the Purpose of Ocean Remote Sensing," IEEE Trans. Geosci. Remote Sens., Vol. 43, No. 6, pp. 1229-1241, June 2005.

[13] Clarizia, M. P., Gommenginger, C.P., Gleason, S.T., Srokosz, M.A., Galdi, C. and M. Di Bisceglie,"Analysis of GNSS-R Delay-Doppler Maps From the UK-DMC Satellite Over the Ocean," Geophys. Res. Lett., 36, L02608, 2009.

[14] Gleason, S.,"Space-Based GNSS Scatterometry: Ocean Wind Sensing Using an Empirically Calibrated Model," IEEE Trans. Geosci. Remote Sens., Vol. 51, No. 9, pp. 4853-4863, 2013.

[15] Unwin, M, Duncan, S., Jales, P., Blunt, P and M. Brenchley, "Implementing GNSS Reflectometry in Space on the TechDemoSat-1 Mission, Proc. Inst. Navigat., Sep. 2014, pp. 12221235.

[16] Gleason S., Lowe S. and Zavorotny V. (2009), Remote Sensing Using Bistatic GNSS Reflections, in GNSS Applications and Methods, S. Gleason and D. Gebre-Egziabher (editors), Artech House (Norwood, MA), 2009.

[17] Zavorotny V., Gleason S., Cardellach E. and Camps A., Tutorial on Remote Sensing Using GNSS Bistatic Radar of Opportunity, IEEE Geoscience and Remote Sensing Magazine, in press, 2014.

[18] Gleason S. (2006), Remote Sensing of Ocean, Ice and Land Surfaces Using Bistatically Scattered GNSS Signals From Low Earth Orbit, Ph.D. Thesis, University of Surrey, 2006.

[19] Jin, S., Cardellach, E. and Xie, F., GNSS Remote Sensing: Theory, Methods and Applications (Remote Sensing and Digital Image Processing), ISBN-13: 978-9400774810, Springer, 2014.

[20] Jales, P.,"Spaceborne receiver design for scatterometric GNSS reflectometry," Ph.D. dissertation, Univ. Surrey, Surrey, U.K., 2012.

[21] Gleason, S., Ruf, C. Clarizia, M.P., OBrien, A. J.,"Calibration and Unwrapping of the Normalized Scattering Cross Section for the Cyclone Global Navigation Satellite System', IEEE Trans. Geoscience and Remote Sensing, Vol. 54, No. 5, May 2016.

[22] MERRByS Product Manual: GNSS Reflectometry on TDS-1 with the SGR-ReSI, Version 3, Surrey Satellite Technology Limited, July 19, 2017. Available at, http://merrbys.co.uk/wp-content/uploads/2017/07/MERRByS-Product-Manual-V3.pdf

[23] Wang, T., Ruf, C., Block, B., McKague, D. S. and S. Gleason, "Design and Performance of a GPS Constellation Power Monitor System for Improved CYGNSS L1B Calibration,' Submitted to IEEE Journal of Selected Topics in Applied Earth Observation and Remote Sensing, Jan. 2018.

[24] DTU Space, National Space Instutute (Denmark). Global Mean Sea Surface.

[25] Marquis, W., The GPS Block IIR/IIR-M Antenna Panel Pattern, Lockheed Martin internal document, publically released, September 2013.

[26] Bar-Sever, Y.,"A new model for GPS yaw attitude," Journal of Geodesy 70:714-723, 1996.

[27] Ruf, C., Gleason, S. and D. McKague, "Assessment of CYGNSS Wind Speed Retrieval Uncertainty," Submitted to IEEE Journal of Selected Topics in Applied Earth Observation and Remote Sensing, JSTARS-2018-00136.R1, Feb. 2018.

[28] Jansen, M.A., Ruf, C.S. and S.J. Keihm (1995), "TOPEX/Poseidon Mircorwave Radiometer (TMR): II. Antenna Pattern Correction and Brightness Temperature Algorithm," IEEE Trans. Geosci. Remote Sens., Vol. 33, No. 1, pp. 138-146, January 1995.

[29] Misra P., and P. Enge, Global Positioning System: Signals, Measurements, and Performance, Ganga Jamuna Press, 2001. ISBN 0-9709544-0-9.

[30] Surrey Satellite Technology Limited, Space GPS Receiver (SGR-5,10,20). Specification can be found at, https://www.sst-us.com/shop/satellite-subsystems/global-positioning-systems-gps-receivers/sgr-10-space-gps-receiver

[31] Ulaby, F. T., Long, D. G., Microwave Radar and Radiometric Remote Sensing, Ann Arbor, MI, USA: Univ. Michigan Press, 2014.

[32] Gleason, S., Gommenginger, C., Cromwell, D., "Fading statistics and sensing accuracy of ocean scattered GNSS and altimetry signals," Advances in Space Research, Vol. 46, Issue 2, July 2010, pp. 208-220.

[33] Cipolini, P., National Oceaonography Center Southampton (U.K.). Personal Communication.

[34] Zavorotny V. and A. Voronovich (2000), "Scattering of GPS Signals from the Ocean with Wind Remote Sensing Application" . IEEE Trans. Geosci. Remote Sens., Vol. 38, pp. 951-964, March 2000. DOI: 10.1109/36.841977

[35] Brown, S.G., "The Average Impulse Response of a Rough Surface and its Applications." Oceanic Engineering, IEEE Journal of. 2. 67- 74. 10.1109/TAP.1977.1141536. 1977

Scott Gleason is a Project Scientist III at the University Corporation for Atmospheric Research in Boulder Colorado. He is a Co-Investigator on the science team and Instrument Scientist for the NASA CYGNSS mission. He received his B.S. degree in Electrical and Computer Engineering from the State University of New York at Buffalo, an M.S. in Engineering from Stanford University and a Ph.D. from the University of Surrey in England. He has worked in the areas of astronautics, remote sensing and Global Navigation Satellite Systems (GNSS) for over 20 years, including at NASA's Goddard Space Flight Center, Stanford's GPS Laboratory, Surrey Satellite Technology Limited, Concordia University and the National Oceanography Centre, Southampton.

Christopher S. Ruf (S85M87SM92F01) received the B.A. degree in physics from Reed College, Portland, OR, and the Ph.D. degree in electrical and computer engineering from the University of Massachusetts at Amherst. He is currently Professor of atmospheric science and space engineering at the University of Michigan; and Principal Investigator of the Cyclone Global Navigation Satellite System NASA Earth Venture mission. He has worked previously at Intel Corporation, Hughes Space and Communication, the NASA Jet Propulsion Laboratory, and Penn State University. His research interests include GNSS-R remote sensing, microwave radiometry, atmosphere and ocean geophysical retrieval algorithm development, and sensor technology development. Dr. Ruf is a member of the American Geophysical Union (AGU), the American Meteorological Society (AMS), and Commission F of the Union Radio Scientifique Internationale. He is former Editor-in-Chief of the IEEE Transactions on Geoscience and Remote Sensing and has served on the editorial boards of Radio Science and the Journal of Atmospheric and Oceanic Technology. He has been the recipient of four NASA Certificates of Recognition and seven NASA Group Achievement Awards, as well as the 1997 TGRS Best Paper Award, the 1999 IEEE Resnik Technical Field Award, the 2006 IGARSS Best Paper Award, and the 2014 IEEE GRSS-S Outstanding Service Award.

Andrew J. O'Brien is a Research Scientist at the Ohio State University ElectroScience Lab. He received his Ph.D. in 2009 in Electrical Engineering from the Ohio State University. From 2005 to 2009, he was a Graduate Research Associate at the Ohio State University ElectroScience Laboratory and worked in the area of adaptive GNSS antenna arrays and precise GNSS receivers on complex platforms. His primary research focus is currently in the area of spaceborne GNSS remote sensing using CYGNSS, TDS-1 and SMAP. Other research activities include GNSS antenna arrays, adaptive antenna electronics, airborne geolocation, and radar systems. Dr. OBrien is a member of the CYGNSS Science Team, and has supported development of end-to-end simulations as well as engineering activities.

Darren S. McKague received the Ph.D. degree in Astrophysical, Planetary, and Atmospheric Sciences from the University of Colorado, Boulder, in 2001. He is an Associate Research Scientist in the Department of Climate and Space Sciences and Engineering at the University of Michigan. Prior to working for Michigan, he worked as a systems engineer for Ball Aerospace and for Raytheon, and as a research scientist at Colorado State University. His work has focused on remote sensing with emphases on the development of space-borne microwave remote sensing hardware, microwave remote sensor calibration techniques, and on mathematical inversion techniques for geophysical retrievals. His experience with remote sensing hardware includes systems engineering for several advanced passive and active instrument concepts and the design of the calibration subsystem on the Global Precipitation Mission (GPM) Microwave Imager (GMI) as well as the development of calibration and inter-calibration techniques for the GPM constellation. His algorithm experience includes the development of a near-real time algorithm for the joint retrieval of water vapor profiles, temperature profiles, cloud liquid water path, and surface emissivity for the Advanced Microwave Sounding Unit (AMSU) at Colorado State University, and the development of the precipitation rate, precipitation type, sea ice, and sea surface wind direction algorithms for the risk reduction phase of the Conical scanning Microwave Imager/Sounder (CMIS).